ELSEVIER

Journal of Materials Processing Technology 167 (2005) 91–102

Journal of Materials Processing Technology

www.elsevier.com/locate/jmatprotec

3D modeling of shear-slitting process for aluminum alloys

Somnath Ghosh*, Ming Li[1], Aniruddha Khadke[2]

Department of Mechanical Engineering, The Ohio State University, Columbus, OH 43202, USA

Received 29 December 2003; received in revised form 1 July 2004; accepted 1 August 2004

Abstract

This work combines experimental studies with finite element simulations to develop a reliable numerical model for simulating the important shearing process in aluminum alloys. Burr formation in shearing is of critical concern with respect to the quality of the product. The paper discusses various aspects leading to the modeling of the shearing process with an aim to design process parameters for burr reduction. Three damage models are implemented in the finite element model for simulating the shearing process. Experiments with macroscopic and microscopic observations are used to characterize the material quantitatively and to calibrate the constitutive and damage models. The user material subroutine VUMAT is used for implementation of material and damage models in the commercial finite element code ABAQUS. Parametric studies are finally conducted to study the effect of process parameters on the shearing process and especially on burr formation.

Keywords: Shear slitting; Burr; Damage models; FEM simulations; Aluminum

1. Introduction

Shearing processes, such as blanking, trimming, piercing, guillotining, etc., are among the most important processes in sheet metal forming operations widely used in various industries like automotive, aerospace and electronics. While research in this area has commonly focused on determination of punch force, punch displacement and energy consumption, critical concerns in many instances are burr formation and resulting quality of cut surfaces. High amount of burr formation leads to numerous problems in industrial applications. In the automotive industry for instance, burrs formed in the trimming process often scratch the surface of the formed parts in the downstream processes. Similar problems associated with the manufacturing of memory discs in the computer industry require specific de-burr operations.

Shear slitting is a manufacturing process to convert a web into multiple narrower webs using rotary blades. It is widely used in cutting-to-width of many materials such as metal, paper and plastics. It is a common process for flat rolled products (FRP) with very thin gage. Applications range from hotline edge-trimming, cold mill edge-trimming, to side trimming and slitting at finishing stage. The processes are required for both ingot source products and continuous cast products.

While shear slitting is generally similar to the normal shearing process, the geometry of the setup is slightly different. The work-piece is passed through a rotary blade and a bottom blade for it to be cut. Schematic diagrams of the blade-setup and different views of the blades are shown in Fig. 1. The entire process occurs in three main stages with respect to deformation and damage mechanisms. The first stage of elastic deformation results in very little bending deformation of the sheet. With stresses reaching the material yield strength, a plastic zone is formed in the clearance region between the blade and the die, where small cracks initiate with continuing blade travel. Subsequently, these cracks grow in size and coalesce to cause final material separation by ductile fracture. As seen in Fig. 2, the fracture surface of the sheet can be divided into four distinct regions, viz. the (a) rollover area, (b) burnish area, (c) fracture area and (d) the burr area. The extent of the burr region depends on the crack path in the final stages of the shearing. This cracking phenomenon by ductile fracture of metals and alloys is quite complex. It depends on

* Corresponding author. Present address: Room 234, 650 Ackerman Road, The Ohio State University, Columbus, OH 43202, USA.
Tel.: +1 6142922599; fax: +1 6142927369.
E-mail address: ghosh.5@osu.edu (S. Ghosh).
[1] Section Head, Process Mechanics, Alcoa Technical Center, PA 15069.
[2] Graduate student, Department of Mechanical Engineering, The Ohio State University.

0924-0136/$ – see front matter © 2004 Elsevier B.V. All rights reserved.
doi:10.1016/j.jmatprotec.2004.08.031

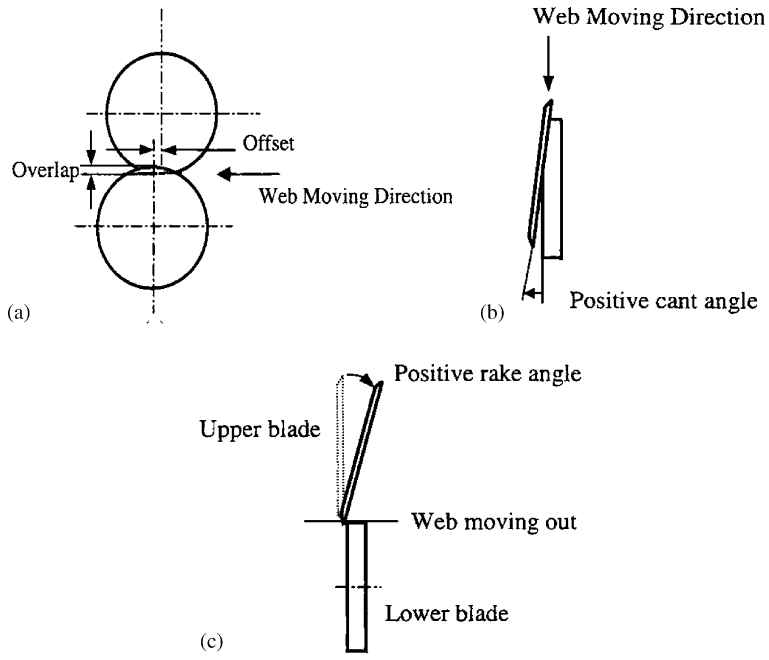

Fig. 1. Schematic diagram of shear-slitting process: (a) side view, (b) top view, and (c) front view.

macroscopic factors such as clearance, cant angle, rake angle, blade sharpness, tooling material, blade geometry, lubricants, cutting line curvature (or geometry), temperature, clamping force, etc. as well as the microstructure of the material.

A major problem with some of these processes is encountered in the quality of the cut-edge, due to burr formation, fines and debris. Various process parameters like clearance, blade overlap, cant angle, rake angle, web speed, web tension, etc. determine this quality for shear-slitting processes. The clearance is the distance between the blade and the lower die cutting edges in horizontal direction. The cant angle is the angle between two blade planes viewed in the direction perpendicular to the web plane, as illustrated in Fig. 1b. Rake angle, shown in Fig. 1c, is the angle between the blade and the bottom blade viewed in the direction parallel to the web plane.

Research in this area of shearing started in the early to mid-1900s and the work by Chang and Swift [1] was one of the first systematic experimental studies on the subject. A comprehensive survey of the progress upto the 1980s has been made by Johnson and coworkers [2,3]. Extensive experimental and analytical work has been made by Atkins [4–6] in this area. Zhou and Wierzbicki [7] have developed a tension zone model while Li's experimental work focused on burr formation and micromechanics of deformation and fracture during shearing process [8,9]. Numerical studies on this subject have been progressing in the last two decades. A major challenge in these simulations is in the prediction of damage and facture. Taupin et al. [12] have used a failure criterion proposed by McClintock [13] for fracture prediction. In this model, the damage parameter is calculated based on the principal stress in the direction of greatest void deformation. Hambli [14,15], and Miguel and Bressan [16] have used the equivalent plastic strain–hydrostatic stress based Le Maitre's model [17], for simulation of blanking process. The Cockroft and Latham model [18], in which the ratio of maximum principle ten-

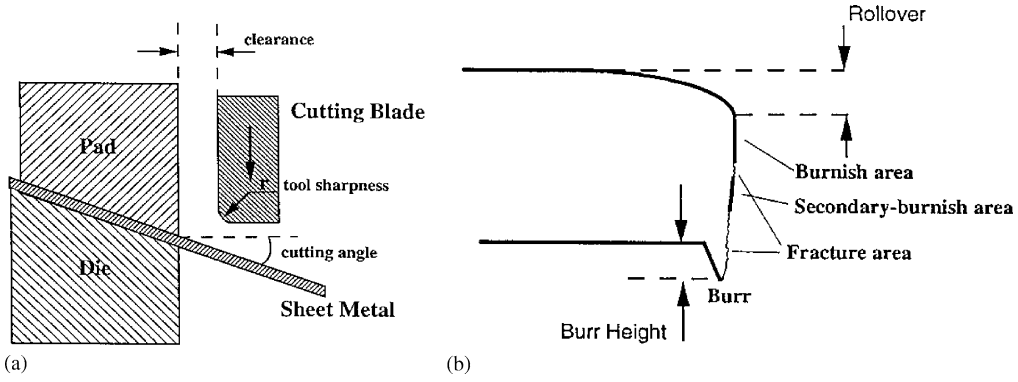

Fig. 2. Schematic of (a) the shearing process and (b) the cut profile.

sile stress to the equivalent stress drives damage evolution, is used in the shearing simulations of Fang et al. [19] and MacCormack and Monaghan [20]. All of these simulations incorporate fracture through an element deletion technique, in which an element is removed once the damage criterion is reached at an integration point. Alternatively, Brokken et al. [21] have used a discrete crack propagation approach for simulation of fracture, in conjunction with the Rice and Tracey's damage model [22]. This model is based on the stress triaxiality, defined as the ratio of hydrostatic stress to the equivalent stress. Brokken et al. [23] have used a modified form of Rice and Tracey's model through different multiplying factors for the stress triaxiality as proposed by Goijaerts et al. [24]. In their work a fracture potential is calculated using the local damage criterion and extrapolated to the nodes in every load increment. When the fracture potential at a node reaches a critical value, a crack is initiated, or in the case of crack tip, propagated in the direction of maximum fracture potential. This direction is determined by sampling a finite number of locations radially spaced in the vicinity of a node. For this approach, a continuous remeshing strategy has to be used in order to accommodate new and moving cracks. Klingenberg and Singh [25] have used the Tvergaard–Gurson model [26,27] for modeling the ductile fracture by void nucleation and growth. Wisselink and Huétink [28] have used the Oyane model [29,30] with a predefined initial crack front. A problem with this method is that the position of the initial crack front is not known in most of the cases. Simulations performed by Kubli et al. [31] include only a shearing operation, which is simulated by continuous remeshing. With this approach, only the rollover zone can be predicted. In most of the work mentioned above, the main emphasis is on the analysis and optimization of the punch force in the blanking process. A majority of these simulations are for the 0° rake angle such as in the blanking operations. However, as shown experimentally [8], the cutting angle (or rake angle) has a dominant effect on burr height. Technology to improve burr height and cut edge quality for non-zero rake angles has been developed [10,11]. Relatively little work is reported on the prediction of crack profile explicitly to minimize the formation of surface defects such as burrs. Current practices of shear slitting of aluminum sheets and foils rely heavily on experience and operators' trial and error procedure.

An effort has been made in this paper to determine the relationship between the slit edge quality and the process parameters. It combines laboratory and field experiments with numerical simulations of the shear-slitting process for developing validated models of the process. The model is subsequently used to examine the influence of the effect of process parameters on the burr formation and hence recommend process design. The finite element model using the commercial code ABAQUS [32] is described in Section 3. Ductile fracture is modeled using three different models, namely the Tvergaard–Gurson model [26,27], the shear failure model [32] and the Cockroft–Latham model [18]. Their effectiveness in modeling the shear-edging process is examined by comparison with experiments. For validation of the damage model, experiments are conducted with normal shearing process with block type knives. The schematic of the normal shearing process with block type knives is shown in Fig. 2a. Macroscopic experiments with microscopic observations are conducted to characterize the material quantitatively and to calibrate the constitutive and damage models. Element deletion method is implemented to represent material separation in these simulations. Parametric studies are done to study the effect of various parameters on the extent of burr formation and the results obtained from simulations are compared with experimental results. Practical experience indicate that among the many process parameters, the most ones are clearance and cant angle. Recent experimental work by Li and coworkers [8,10] has found that rake angle can significantly contribute to burr height. Therefore, the paper focuses on the simulation of the effects of rake angle and cant angle.

2. Material constitutive and damage models

2.1. Constitutive model

The aluminum alloys Al6022T4 and Al5182-H19 are provided by Alcoa Technical Center and are modeled using finite deformation elastic–plastic constitutive relations in ABAQUS-Explicit [32] with experimental validation. The hardening parameter H in the elastic–plastic model is expressed in terms of the flow stress σ_y and the plastic work W_p by

$$H = \frac{2}{3}\sigma_y \frac{d\sigma_y}{dWp} \quad (1)$$

In each increment of the ABAQUS simulations, instantaneous values of H are obtained as the gradient of the experimental stress–plastic strain curve obtained from uniaxial tension tests of specimens, as shown in Fig. 3. From these experiments, the elastic modulus of the alloy Al6022T4 is found to be $E = 64 \times 10^3$ MPa and the yield stress $\sigma_y = 161$ MPa. The material properties for the alloy Al5182-H19 are $E = 64 \times 10^3$ MPa and the yield stress $\sigma_y = 327$ MPa.

2.2. Damage models

Macroscopic damage models are necessary to predict the onset and propagation of ductile fracture to cause material separation. A major mechanism of the initiation of ductile fracture in metals is void nucleation caused by dislocation pile-ups, second phase particle cracking or other imperfections. Under the influence of plastic deformation, the voids subsequently grow with coalescence to form a dominant crack [19]. Various damage laws, which predict the onset of failure based on functions of stresses and strain history, have been proposed in literature. Of these, the models commonly used for ductile fracture are by Clift et al. [33],

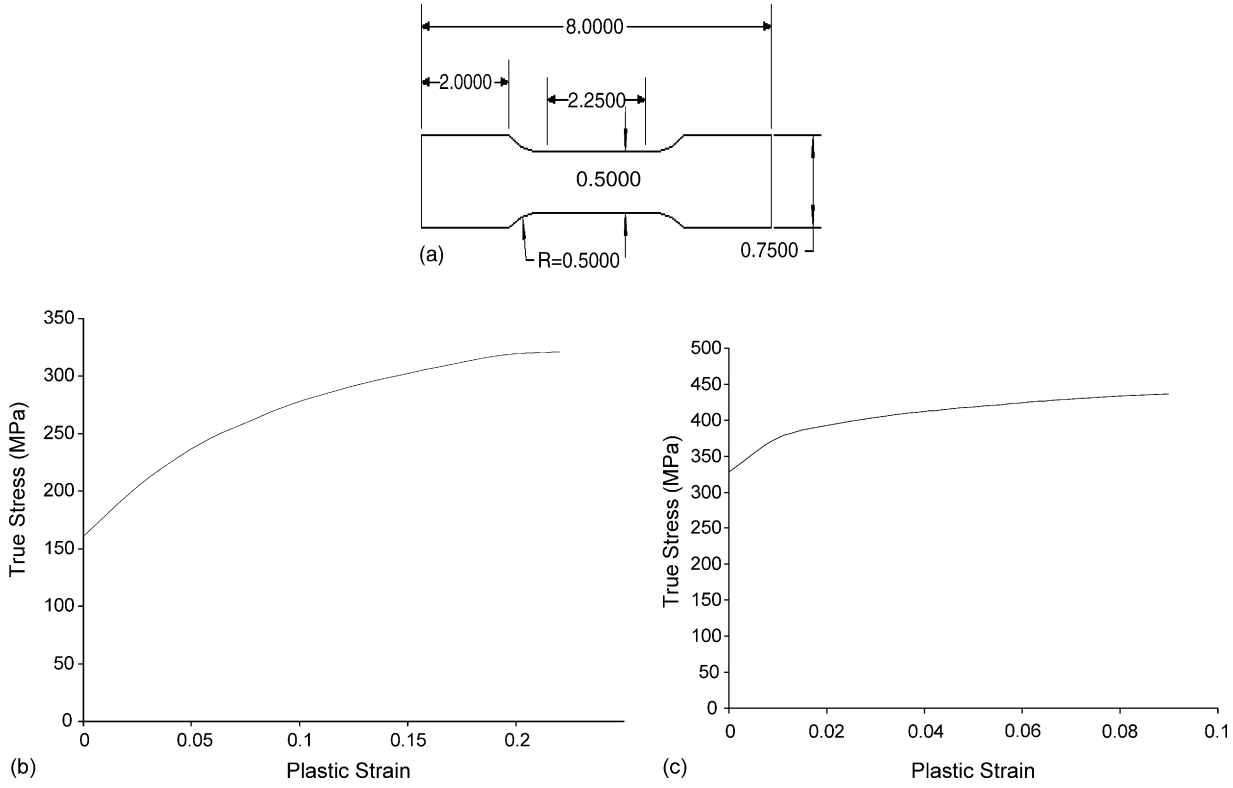

Fig. 3. (a) Dimensions of the dog-bone specimen of unit thickness (in inches), (b) true stress–plastic strain response of the aluminum alloy Al6022T4, (c) true stress–plastic strain response of the aluminum alloy Al5182-H19.

Tvergaard–Gurson [26,27], Rice and Tracey [22], McClintock [13], Oyane [29,30] and Cockroft and Latham [18]. In many of these models, a material point is assumed to have failed when a local damage parameter reaches a certain critical value. For many shearing operation simulations, the damage parameter is calculated based on the equivalent plastic strain and some function of the stress tensor, e.g. stress triaxiality, hydrostatic stress, principal stress, etc. An alternative accumulated equivalent plastic strain based shear failure model, featured in ABAQUS [32] is also a viable model of ductile fracture. In this paper, three different damage models are calibrated and validated with experiments for determining their suitability in the shearing simulations. They are (i) the Tvergaard–Gurson model, (ii) the Cockroft–Latham model and (iii) the shear failure model. The analyses use the element deletion technique, in which the element stress-carrying capacity is reduced to zero at a critical damage, in conjunction with these models to represent material separation and crack propagation. A brief description of the damage models is given below.

2.2.1. Tvergaard–Gurson model

The Tvergaard–Gurson model [26,27] of void nucleation, growth and coalescence is based on the principle of formation of microscopic voids and growth of existing voids with increasing plastic strain. The void volume fraction is used as the damage parameter and a pressure dependent yield function is defined in this model as:

$$\phi = \left(\frac{q}{\sigma y}\right)^2 + 2q_1 f \cos h\left(-q_2 \frac{3p}{2\sigma y}\right) - (1 + q_3 f^2) = 0 \tag{2}$$

where q is the effective Mises stress, p the hydrostatic pressure, f the void volume fraction, σ_y the yield stress of the matrix material and q_1, q_2, q_3 are the experimentally evaluated constants. The rate of change of void volume fraction is governed by the equations

$$\dot{f} = \dot{f}_{\text{gr}} + \dot{f}_{\text{nucl}} \text{ with } \dot{f}_{\text{gr}} = (1 - f)\dot{\varepsilon}^{\text{pl}} : I \text{ and } \dot{f}_{\text{nucl}} = A\dot{\bar{\varepsilon}}^{\text{pl}} \tag{3}$$

where $\dot{f}_{\text{gr}}$ is the change in volume fraction due to growth of existing voids and $\dot{f}_{\text{nucl}}$ the change in volume fraction due to nucleation of new voids. The nucleation parameter A is defined in [26] as

$$A = \frac{f_{\text{N}}}{S_{\text{N}}\sqrt{2\pi}} \exp\left[-\frac{1}{2}\left(\frac{\bar{\varepsilon}^{\text{pl}} - \varepsilon_{\text{N}}}{S_{\text{N}}}\right)\right] \tag{4}$$

where ε_{N} and s_{N} are the mean and standard deviation of the nucleating strain distribution and f_{N} is the volume fraction of nucleating voids. When the void volume fraction reaches a critical value f_{c}, the model assumes void coalescence with accelerated void growth. In this phase, material starts to soften till the void volume fraction reaches a value f_{f}. At this fraction,

there is a complete loss of stress-carrying capacity and the yield surface reduces to a single point. An element, for which all integration points have failed, is subsequently removed from the analysis.

2.2.2. Cockroft–Latham model

This model, suggested by Cockroft–Latham [18] and Oyane [29,30], determines the likelihood of fracture from tensile plastic deformation, by consideration of plastic work to failure. The material is assumed to undergo ductile fracture when a damage parameter $\boldsymbol{D}$ reaches a critical value $\boldsymbol{C}$, where

$$\boldsymbol{D} = \int_0^{\bar{\varepsilon}^{\mathrm{pl}}} \left(\frac{\sigma^*}{\bar{\sigma}} \right) \mathrm{d}\bar{\varepsilon}^{\mathrm{pl}} \tag{5}$$

and $\bar{\varepsilon}^{\mathrm{pl}}$ is the equivalent plastic strain, $\bar{\sigma}$ is the effective Von-Mises stress and σ^* is the maximum positive principal stress. The material loses its stress-carrying capacity at the fracture plastic strain $\bar{\varepsilon}_{\mathrm{f}}^{\mathrm{pl}}$. This model is implemented in ABAQUS-Explicit [32] using the user material subroutine VUMAT. This model has been used by Fang et al. [19], MacCormack and Monagham [20] for blanking and trimming operations.

2.2.3. Shear failure model

The shear failure model uses the accumulated equivalent plastic strain as a damage indicator and predicts the occurrence failure when a damage parameter w exceeds 1 (see [32]), where

$$w = \sum_n \left(\frac{\Delta\bar{\varepsilon}^{\mathrm{pl}}}{\bar{\varepsilon}_{\mathrm{f}}^{\mathrm{pl}}} \right) \tag{6}$$

and $\Delta\bar{\varepsilon}^{\mathrm{pl}}$ is the increment of equivalent plastic strain, $\bar{\varepsilon}_{\mathrm{f}}^{\mathrm{pl}}$ the plastic strain at failure that can be a function of the plastic strain rate, stress triaxiality and temperature, and the summation is performed over n increments in the analysis. In the present analysis, only the stress dependence of $\bar{\varepsilon}_{\mathrm{f}}^{\mathrm{pl}}$ is assumed.

3. Experiments for calibration of material models

3.1. Mechanical testing and metallography

Material parameters for the aluminum alloy Al6022T4 are evaluated using two sets of experiments. In the first set, tension tests are conducted with ASTM standard dog-bone specimens of the sheet with dimensions shown in Fig. 3a. The dog-bone samples are strained to failure at a constant rate of 5×10^{-4} in./s on an Instron 2000 mechanical testing system. Load data is sampled directly from the load cell and strain is recorded using a 1 in. extensometer placed across the center of the sample. The specimen widths are slightly reduced near the center to ensure fracture within the range of the extensometer. Four samples of identical dimensions are tested under same conditions to ensure repeatability and macroscopic load–displacement response curves are generated. To facilitate microscopic observations for some damage models like the Tvergaard–Gurson model, a second set of experiments is carried out using U-notched specimens of the sheet metal as shown in Fig. 4a. The experiments are designed to measure the evolving void volume fraction at regions of interest. The specimens are strained at a rate of 5×10^{-4} in./s, and the load is measured using a load-cell on the MTS, while the strain on each specimen is measured using a 1 in. extensometer. Three samples are initially strained to failure and the failure strain is determined from the extensometer readings to be approximately 11.3%. A number of other specimens are subsequently loaded to different levels of pre-failure strains, at which loads are interrupted. Following load interruption, each specimen is sectioned to extract samples from the notched regions to study the regions around each notch and at the center of each specimen. These samples are mounted and polished using standard metallographic techniques and photomicrographs of each sample are taken with a Philips XL-30 ESEM. Fig. 4b shows the micrograph near the edge at 11% strain level at a scale of 20 μm. It is apparent that discrete voids have initiated in the microstructure at this strain. This void evolution infor-

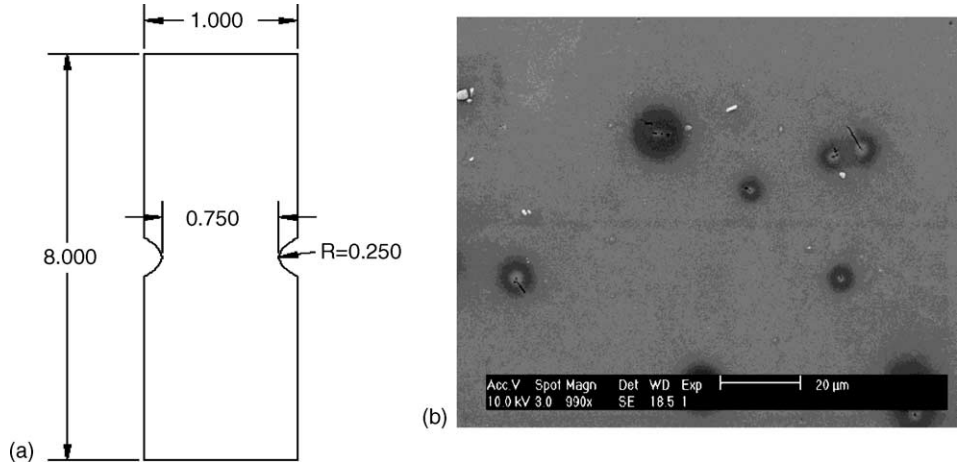

Fig. 4. (a) Dimensions of the notched specimen (in inches) and (b) sample micrograph near the notch at 11.2% strain.

mation is necessary for the calibration of constitutive model parameters in the Tvergaard–Gurson model.

Microstructural characterization and analysis of the evolved voids are necessary for calibrating the Tvergaard–Gurson model. The actual microstructural geometry of the voids is generally quite complex and an exhaustive database is required to store all the geometric details. To avert this, equivalent microstructures of equivalent ellipses that closely approximate the actual morphology but are computationally less demanding, are generated. This process has been successfully developed in [34]. The digitized image data is first transferred into binary format to distinguish between the voids and matrix phases. The zeroth (I_0), first (I_x, I_y) and second (I_{xx}, I_{yy}) order geometric moments are then computed for each void by adding the contributions from each pixel that lies within the void boundary. The centroidal coordinates (x_c, y_c) of the equivalent ellipse is first evaluated from the zeroth and first order moments as: $x_c = I_x/I_0$, $y_c = I_y/I_0$,. The major and minor axes of the equivalent ellipsoids are then obtained equating the second moments of the ellipses with the pixel-based moment data. The size of each void in the micrograph is retained in the form of major and minor axes of the ellipse. This simplification of the particle data allows for simple statistical analysis of the system. It enables easy computations of local volume fraction of the voids in the matrix.

3.2. 3D Volume fraction from 2D data using stereology

For effective comparison with 3D computational models, the microstructural data and material characterization (e.g. size and shape distribution of ellipses) of 2D sections of the specimen have to be mapped to 3D microstructural representations. Methods of stereology enable the mapping of certain 3D characteristics from 2D projected data of the microstructure [35]. For example, distribution of 3D spheroids in the microstructure can be estimated from the size and shape distribution of 2D elliptical cross-sections. Following developments in [34,35], modified Saltykov transformation is used in this study to obtain 3D void volume fraction by incorporating shape effects for generating prolate or oblate spheroid geometries from known distributions of elliptical cross-sections. The 3D spheroid size–shape distribution is obtained from the 2D size–shape distribution [35] as:

$$N_v(i, j) = \frac{1}{\Delta} \sum_{\alpha=i}^{m} \sum_{\beta=j}^{k} p^{i\alpha} N_A(\alpha, \beta) q^{j\beta} \tag{7}$$

The range of 2D ellipses and the 3D spheroids is divided into m intervals. The size of the interval Δ, for prolate spheroids is $\Delta = B/m$ and for oblate spheroids is $\Delta = A/m$, where B is the largest of all minor axis lengths (b) and A is largest of all major axis lengths (a). A shape parameter (or square eccentricity) defined as $y^2 = 1 - (b/a)^2$ is also recorded and divided into k intervals of equal size $1/k$. Then $N_v(i, j)$ is the number of prolate or oblate spheroids in the ijth size–shape interval and $N_A(\alpha, \beta)$ is the number of ellipses in the size–shape interval $\alpha\beta$. The coefficients $p^{i\alpha}$ and $q^{\beta j}$ for the prolate and oblate categories are taken from tables provided in [35]. Void volumes for each interval ij are obtained from the mean size $(i–0.5)\Delta$ and mean shape parameter $(j - 0.5)/k$ and the total volume of voids is calculated by adding the volumes from all intervals. The void volume fraction near the notch is calculated for specimens loaded to different strain levels using this method. Micrographs are taken at three different locations near the edge and the average value of void volume fraction are calculated and tabulated in Table 1. The void volume fraction is observed to increase with overall strain level in an exponential manner as described in the Tvergaard–Gurson model.

Table 1
Void volume fraction at the notch edge as a function of the overall strain

Overall strain (%)	Void volume fraction
8	3.52E−04
9	9.62E−05
10	1.75E−03
11	8.23E−04
11.2	3.40E−03
11.25	1.91E−02

3.3. Damage parameter evaluation

An inverse method, involving numerical simulations and experiments, is implemented to evaluate damage parameters in various models of ductile fracture used in the simulation of the shearing process. For the Tvergaard–Gurson model, the damage parameters include f_c and f_f as well as the nucleation parameters ε_N, s_N and f_N, while for the Cockroft–Latham model the parameter is C, and the failure plastic strain $\bar{\varepsilon}_f^{pl}$ is the damage parameter for the shear failure model. The experimental load–displacement curve showing failure in the dog-bone specimens for the first set of experiments is depicted in Fig. 5. In the ABAQUS finite element model to simulate these experiments, only a quarter of the specimen is modeled using QUAD4 plane stress elements with the material model developed in Section 2.1. A very small geometric imperfection is introduced in the model to start necking at the center of the specimen. The damage parameters in each model of ductile fracture are adjusted such that the results of the simulation match the experimental results. For the Tvergaard–Gurson model, the calibration process yields $f_c = 0.08$ and $f_f = 0.1$; for the Cockroft–Latham model $C = 0.6$ and for the shear failure model $\bar{\varepsilon}_f^{pl} = 0.35$. The comparison of the simulation and the experimental results using these damage values is shown in Fig. 5. The corresponding crack profiles with the damage models are compared with the experimental crack in the dog-bone sample in Fig. 6. For modeling shear slitting of the aluminum alloy Al5182-H19, the results from the uniaxial tension tests in Fig. 3b are used. The equivalent plastic strain at failure for the shear failure model is found to be $\bar{\varepsilon}_f^{pl} = 0.29$.

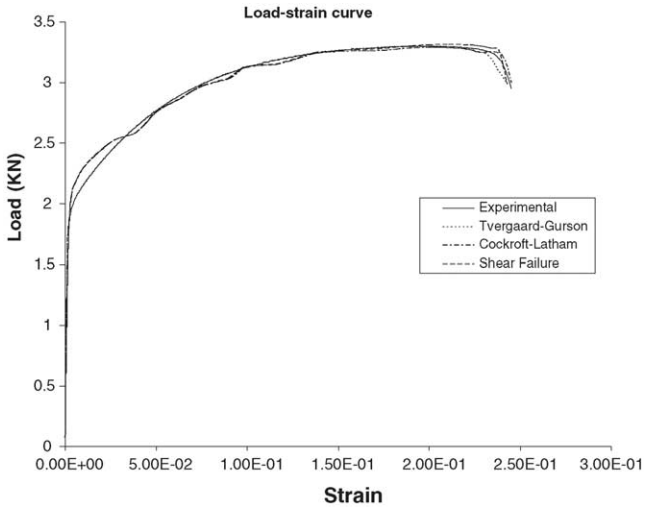

Fig. 5. Load–strain experimental curve for the dog-bone specimen showing failure with simulated results of three damage models.

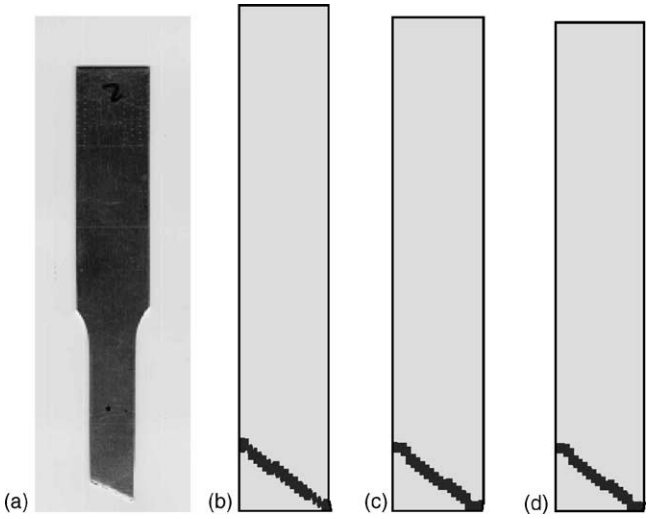

Fig. 6. Crack profiles in the dog-bone sample for: (a) experiment, (b) simulations with the Tvergaard–Gurson model, (c) simulations with the Cockroft–Latham model, (d) simulations with the shear failure model.

A plot of the corresponding equivalent plastic strain for this model, showing the plastic localization region is presented in Fig. 7b.

Additionally, the Tvergaard–Gurson model requires the evaluation of the nucleation parameters ε_N, s_N and f_N. These are calibrated from the microscopic void volume fraction data as a function of overall strain, obtained from the set of experiments with notched specimens. The genetic algorithm (GA) [36,37] is used to minimize the difference between simulated and experimental void volume fraction in a least square sense, given by the fitness function

$$f = \sum_{i=1}^{\text{ndata}} ||f^* - f(\varepsilon^*, v)||^2 \tag{8}$$

where f^* is the void volume fraction and ε^* the corresponding strain. The fitness function in GA converges to the minimum value with an optimum set of parameters. The values of the nucleation parameters are obtained as $\varepsilon_N = 0.5$, $s_N = 0.1$ and $f_N = 0.04$. Fig. 7a shows the void volume fraction as a

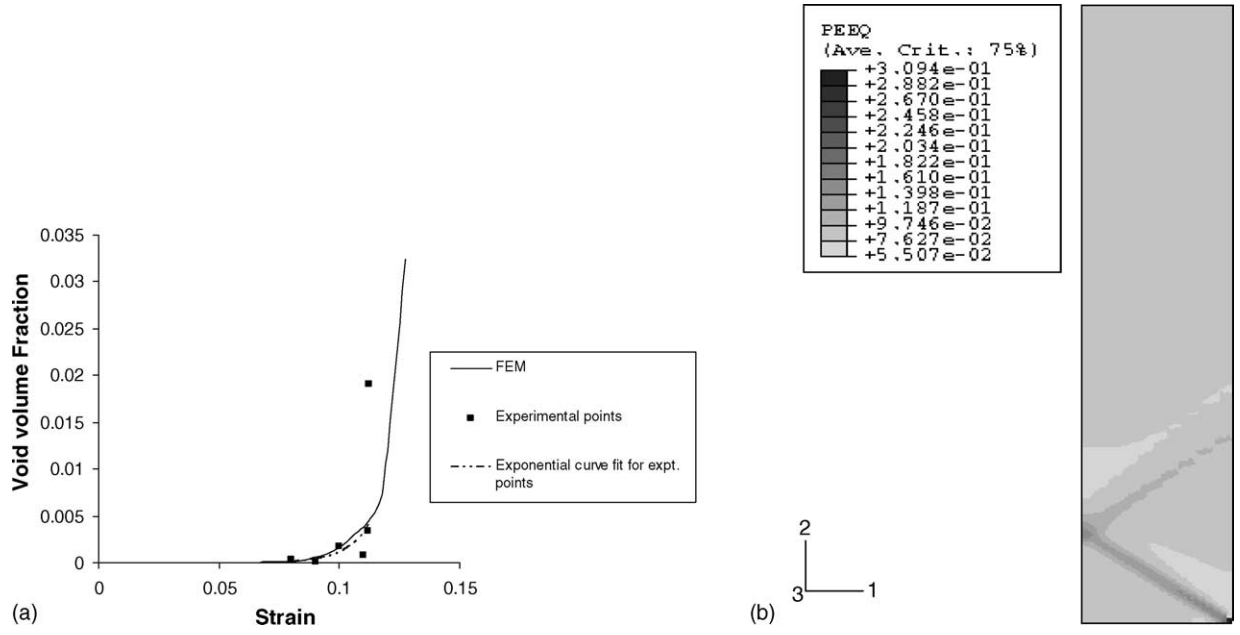

Fig. 7. (a) Void volume fraction as a function of the overall strain for experiments and simulations with the Tvergaard–Gurson model. (b) Plot of equivalent plastic strain in the dog-bone specimen of Al5182-H19 at experimentally observed overall strain at fracture.

function of the strain for experiments and simulation. The discrete experimental points correspond to each interrupted load test, of which one corresponds to a localization instability region where the void volume fraction is growing rapidly. A continuous function, represented by an exponential expression, is fit to the discrete data and compared with the simulation. Given the various factors that contribute to the errors due to interrupted testing and stereology, the simulation predictions are found to match the experimental data quite well.

4. Validation of damage models

It is important that the effectiveness of each damage model in simulating the shearing and shear-slitting process be established, prior to their application in the actual field problems. In this effort, the results of simulations with the three damage models are compared with experiments on the shearing process with block type blades as shown in Fig. 2a. The width (out of plane dimension) of the aluminum sheets is very large compared to the thickness and hence, a 2D plane strain computational model is set up. The model is restricted to cases where the edge of the cutting tool is parallel to the width of the sheet, avoiding any skewness in the cuts. The clamping pad, die and the blade shown in Fig. 2 are modeled as rigid surfaces. The metal sheet of dimensions 1 mm × 2 mm is meshed using approximately 7000 plane strain QUAD4 (CPE4R) elements in ABAQUS/Explicit as shown in Fig. 8.

The results of numerical simulations with the Tvergaard–Gurson model, the Cockroft–Latham model and the shear failure model are shown in Fig. 9. Also the part and the scrap profiles from experiments are shown in Fig. 9d. For the Tvergaard–Gurson model, the material does not separate and the crack propagation arrests in the thickness direction on account of very small increase in the hydrostatic stresses and dilatational strains in this process. Hence, it is concluded that the expected material separation in shearing problems cannot be modeled successfully with the Tvergaard–Gurson model. The Cockroft–Latham model however develops complete material separation due to crack propagation as shown in Fig. 9b. When the simulated crack profile is compared with the experimental profile in Fig. 9d, a significant difference is observed. Also, the burr heights obtained from the simulations using the Cockroft–Latham model do not match with the experimental results for different values of clearance, tool radius and cutting angle. For all the cases, the crack propagates and ends very near the corner of the bottom blade which does not yield the experimentally observed burr height. This model is consequently considered inappropriate with respect to the objectives of this study. Finally, the material separation and crack propagation is found to be successfully modeled using the shear failure model. As shown in Fig. 9c, the simulated crack profile using this model compares well with the experimental result. Additionally, the simulated burr heights generally agree with the experimental observations. This confirms the suitability of the shear failure model for shearing process simulations.

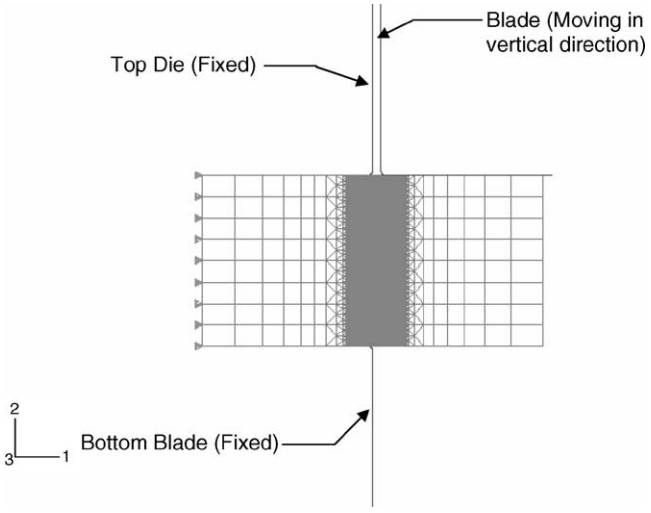

Fig. 8. The finite element model setup of the edge shearing problem in ABAQUS explicit.

5. 3D finite element model of the shear-slitting process

The aluminum alloy AL5182H19 is commonly subject to shear slitting at Alcoa. The finite element model for the shear-slitting process is developed using the commercial code ABAQUS/Explicit [32] with the user material subroutine VUMAT. Due to the nature of boundary conditions, geometry of the setup, e.g. the variations in cant and rake angles, the model is developed in 3D. The clamping pad, and the blades are modeled as rigid surfaces. It is the experience of the Alcoa researchers that the effects of tooling material are from friction and wearing perspective, not from elastic deformation perspective. It is assumed that rigid blades (both top and bottom blades) have little effect on the cutting edge quality. The metal sheet of dimensions 0.2159 mm × 2 mm × 6 mm is meshed using approximately 160,008-noded brick elements (C3D8) as shown in Fig. 10. A graded mesh that facilitates high gradients in a very narrow region near the cutting tool is used to account for localized deformation and stresses. Excessive element distortion can take place in the simulation, since it involves large deformations with complex phenomena like sharp contact and material fracture. Loss of element accuracy and/or misrepresented boundary conditions can lead to high degrees of inaccuracy and inefficiency, sometimes causing termination of the analysis. To overcome this in the present analysis, the arbitrary Lagrangian–Eulerian (ALE) option in ABAQUS/Explicit [32] is used. It combines the features of pure Lagrangian analysis and Eulerian analysis and avoids excessive element distortion and contact surface penetration for the shearing problems.

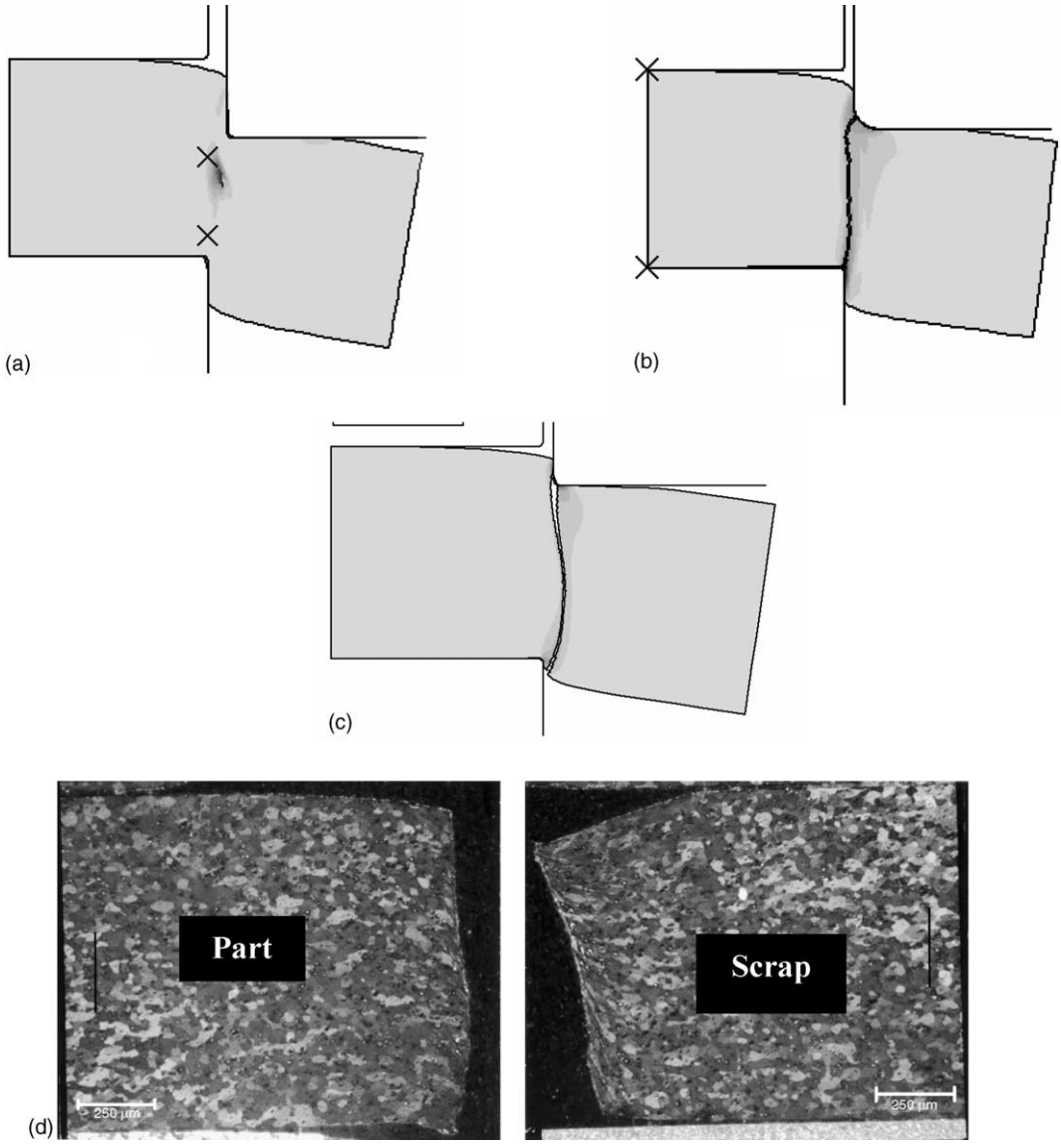

Fig. 9. Results of simulation of the shearing process for 5% clearance, 0.025 mm blade radius and 0° cutting angle: (a) contour plot of void volume fraction with the Tvergaard–Gurson model showing arrested cracking; (b) contour plot of equivalent plastic strain with the Cockroft–Latham model; (c) contour plots of equivalent plastic strain at 0.18 mm blade travel with the shear failure model; and (d) experimentally obtained micrographs of the sheared region.

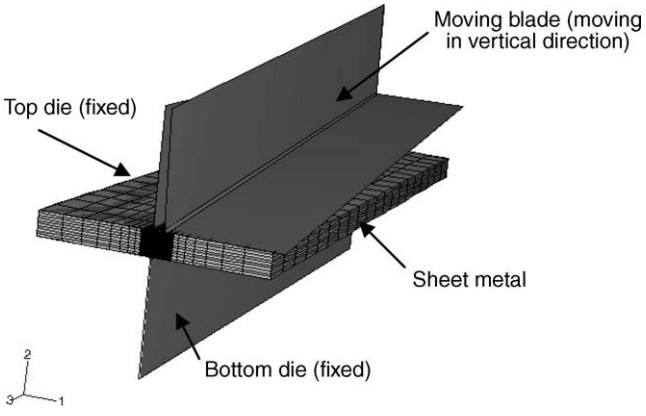

Fig. 10. FE model setup for the shear-slitting process.

The material properties for the AL5182H19 alloy are discussed in Section 2. Based on the observations made in the 2D shearing process simulations, the shear failure model with the calibrated critical shear strain $\bar{\varepsilon}_{\mathrm{f}}^{\mathrm{pl}} = 0.29$, is used in these simulations. The rigid die and clamping pad are assumed to be totally constrained. For the blade, translation in horizontal direction as well as rotation is constrained and a velocity boundary condition of 0.5 m/s is specified for the blade in vertical direction. Contact between the rigid surfaces and the metal sheet is modeled using surface-to-surface contact with a penalty formulation in ABAQUS. A Coulomb friction model is used to represent friction between contacting surfaces. A friction coefficient $\mu = 0.05$ is arrived at by comparing the results of simulations with experimental results. The deformed configuration for the process simu-

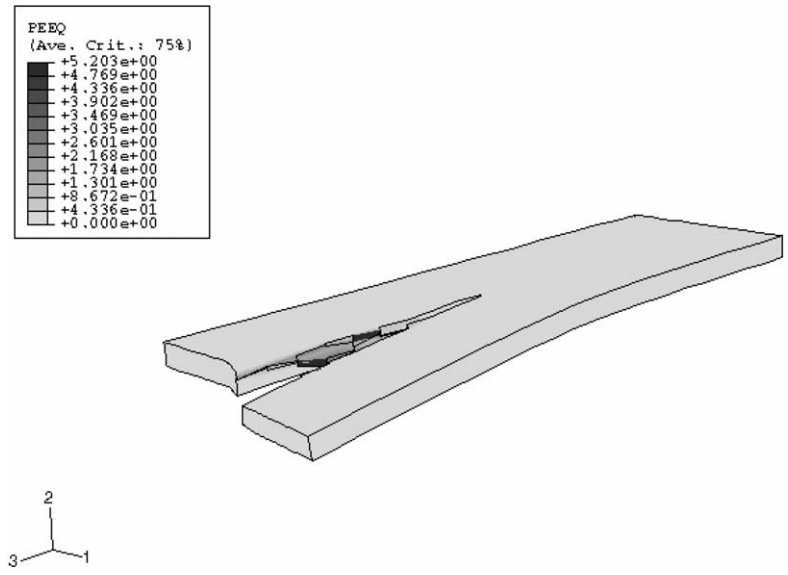

Fig. 11. Deformed configuration for shear-slitting process for 0° rake angle and 0° cant angle.

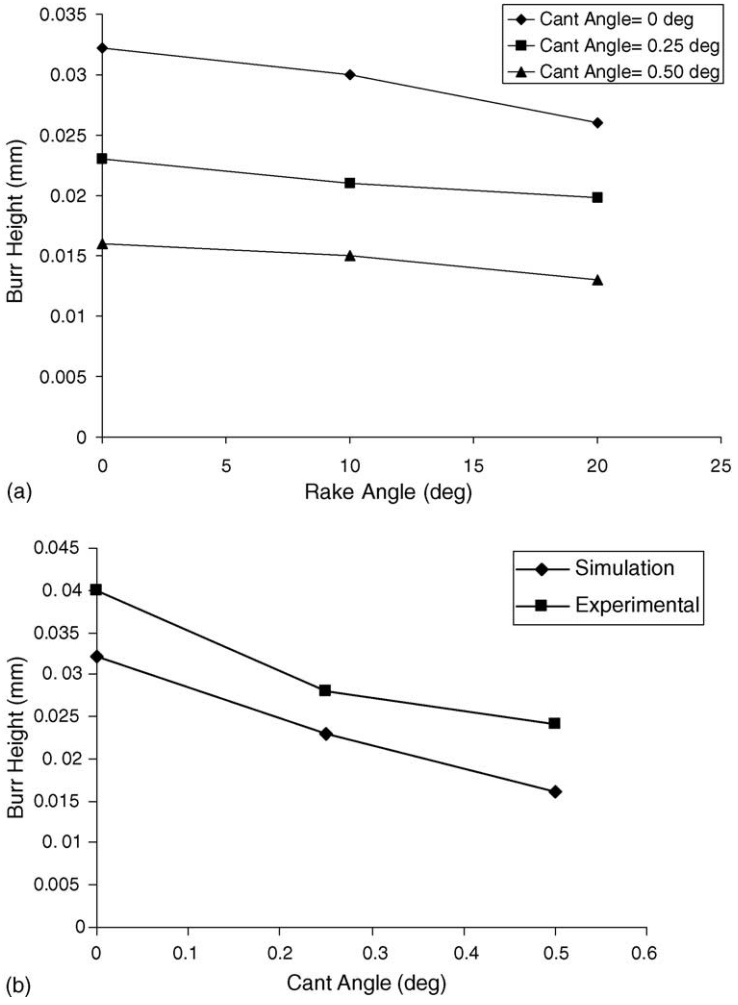

Fig. 12. (a) Plot of burr heights for different rake angles and cant angles. (b) Comparison of burr heights obtained from simulation with experimentally observed burr heights for different cant angles.

lation with 0° rake angle and 0° cant angle is shown in Fig. 11.

5.1. Parametric studies for burr formation in shear slitting

The extent of burr formation in the shear-slitting process depends on various process parameters such as the cant angle, rake angle, clearance, etc. To understand the effect of these process parameters, a systematic parametric study with the finite element model is conducted. The effect of variations in the rake angle and the cant angle on the extent of burr formation is studied. The simulations are conducted for three different rake angles of 0°, 10° and 20° and for three cant angles of 0°, 0.25° and 0.5°. The burr height from the simulation is measured at different locations over the cut-edge in the *z*-direction and the mean result of all these values is used as the final burr height to be compared with experiments. Fig. 12a shows the plot of burr heights for different rake angles and different cant angles. The burr height decreases with increasing rake angle and is a minimum near a rake angle of 20°. This effect of the rake angle on the burr height is similar as the effect of cutting angle on the burr height in shearing processes. The rake angle introduces a normal component of cutting force, which accelerates the crack initiation and growth. Due to this, the crack propagates faster through the thickness of the sheet, resulting in reduction in burr height. From Fig. 12a it is also be seen that the burr height decreases as the cant angle increases. The values of the burr heights from the simulation for different cant angles are compared with the values obtained from the experiments, which are conducted for cant angles of 0°, 0.25° and 0.5°. The comparison of the simulation and experimental results is shown in Fig. 12b. The simulated values of the burr height are about 15–18% lower than the experimental values. This difference can arise due to errors in the measurements, lack of proper lubrication and temperature effects in the model and also due to the fact that slitting is being simulated in this work using continuum damage laws, etc. However, both of them show similar trends in burr heights reduction as a function of cant angle.

The effect of material properties on the burr height is studied next with added simulations for Al6022-T4 alloy, for which the material and damage properties are discussed in Sections 2 and 3. The simulations were performed for 0° rake angle and different cant angles. The comparison of the burr heights for the two materials at different cant angles is shown in Fig. 13. The burr heights for the Al5182-H19 alloy are slightly less than the burr heights obtained using the Al6022-T4 alloy. This can be explained from the fact that the equivalent plastic strain at failure for Al5182-H19 is lower than that of Al6022-T4, implying lower ductility for the latter material. The extent of burr formation is hence found to be directly related to the ductility of the material and is lower for materials with lower strain to failure values.

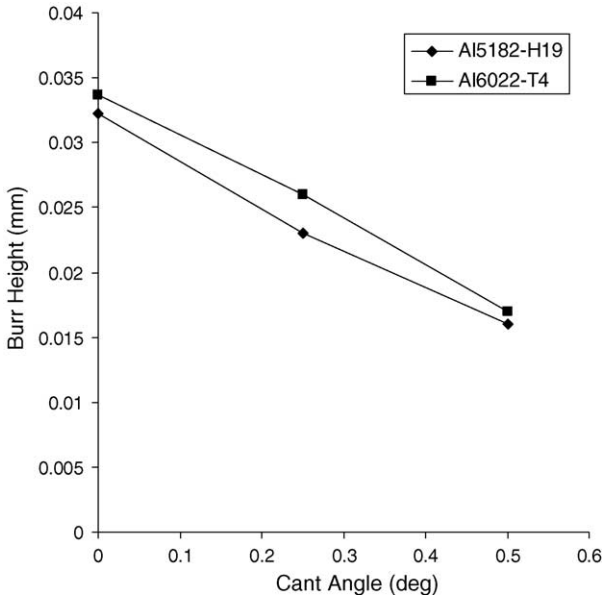

Fig. 13. Comparison of burr heights for the Al5182-H19 and Al6022-T4 alloys for 0° rake angle.

6. Conclusions

Shearing process simulations are conducted for aluminum alloys in this study by combining experiments with modeling for validation. The objective of this work is to understand the effect of various process parameters on the extent of burr formation in the shear-slitting processes in an attempt to reduce burr formation in the production cycle. The material properties for the simulations are obtained from experiments performed on two aluminum alloys, namely Al5182-H19 and Al6022-T4, at Alcoa Technical Center. A major challenge in modeling the shearing process is to model the ductile fracture. Different damage models are considered in this study and are validated using extensive macroscopic and microscopic observations from experiments on ductile fracture. It is observed that the shear failure model is the most suitable model for the numerical simulations in comparison with the Tvergaard–Gurson model and the Cockroft–Latham model. The latter models do not predict the cut-surface profile as observed in the experimental studies. Experimental verification of results confirms that the shear failure model describes the shearing process with satisfactory accuracy due to the dominant shearing mode in this process. Macroscopic numerical simulations with the material and damage model are reasonably successful in predicting the cut-surface profile and burr heights for the shear-slitting process. The simulation responds to parameter changes such as rake and cant angles, showing the same trends of dependence of burr height as experiments. The results give an estimate of the process parameters necessary for minimizing the burr formation. Additionally, the ductility of material is also found to affect the development of burr. While this study demonstrates a robust approach for modeling the shear-slitting process, more

sophisticated techniques such as cohesive zone models or multi-scaled analysis can be used to study the effect of material microstructure on the process. Such developments are currently under consideration.

Acknowledgements

This work has been supported by the National Science Foundation through grant no. DMI-9912547 (Program Director: Dr. Delcie Durham and Dr. Julie Chen) and by a grant from Alcoa Technical Center. The authors are grateful to Alcoa Technical Center Staff for providing some of the experiments. Computer support by the Ohio Supercomputer Center through grant no. PAS813-2 is also acknowledged.

References

[1] T.M. Chang, H.W. Swift, Shearing of metal bars, J. Inst. Metals 78 (1950) 393.
[2] W. Johnson, R.A. Slater, Survey of slow and fast blanking of metals at ambient and high temperatures, in: Proceedings of the International Conference on Manufacturing Technology, CIRP-ASTME, 1967, p. 825.
[3] W. Johnson, S.K. Ghosh, S.R. Reid, Piercing and hole-flanging of sheet metals: a survey, Memoires Scientifiques Revue Netallurgie 77 (1980) 585.
[4] G. Atkins, On cropping and related process, Int. J. Mech. Sci. 22 (1980) 215.
[5] G. Atkins, On the mechanics of guillotining ductile metals, J. Mater. Proc. Tech. 24 (1990) 245.
[6] G. Atkins, Surface produced by guillotining, Phil. Mag. A 43 (1981) 827.
[7] Q. Zhou, T. Wierzbicki, A tension zone model of blanking and tearing of ductile metal plate, Int. J. Mech. Sci. 38 (1996) 303.
[8] M. Li, An experimental investigation on cut surface and burr in trimming aluminum autobody sheet, Int. J. Mech. Sci. 42 (5) (2000) 889–906.
[9] M. Li, Micromechanisms of deformation and fracture in shearing aluminum alloy sheet, Int. J. Mech. Sci. 42 (5) (2000) 907–923.
[10] M. Li, G. Fata, Trimmed Aluminum Sheet, US Patent 5,820,999 (1998).
[11] M. Li, G. Fata, Method and Apparatus for Trimming Aluminum Sheet, US Patent Application Publication, US 2002/0017173 Al (February 14, 2002).
[12] E. Taupin, J. Breitling, W. Wu, T. Altan, Material fracture and burr formation in blanking results of FEM simulations and comparison with experiments, J. Mater. Process. Technol. 59 (1996) 68–78.
[13] F.A. McClintock, Criteria for ductile fracture by the growth of holes subjected to multiaxial stress states, Trans. ASME J. Appl. Mech. 35 (1968) 363–371.
[14] R. Hambli, FEM fracture prediction during sheet metal blanking processes, Eng. Fracture Mech. 68 (2001) 365–378.
[15] R. Hambli, Prediction of burr height formation in blanking using neural networks, Int. J. Mater. Sci. 44 (2002) 2089–2102.
[16] V. Miguel Jr., J.D. Bressan, A computational approach to blanking processes, J. Mater. Process. Technol. 125/126 (2002) 206–212.
[17] J. Lemaitre, A continuous damage mechanics model for ductile fracture, J. Eng. Mater. Technol. 107 (1985) 83–89.
[18] M.G. Cockroft, D.J. Latham, Ductility and workability of metals, J. Inst. Metals 96 (1968) 33–39.
[19] G. Fang, P. Zeng, L. Lou, Finite element simulation of the effect of clearance on the forming quality in the blanking process, J. Mater. Process. Technol. 122 (2002) 249–254.
[20] C. MacCormack, J. Monaghan, Failure analysis of cold forging dies using FEA, J. Mater. Process. Technol. 117 (2001) 209–215.
[21] D. Brokken, W.A.M. Brekelmans, F.P.T. Baaijens, Predicting the shape of blanked products: a FEM approach, J. Mater. Process. Technol. 103 (2000) 51–56.
[22] J.R. Rice, D.M. Tracey, On the ductile enlargement of voids in triaxial stress fields, J. Mech. Phys. Solids 17 (1969) 201–217.
[23] D. Brokken, W.A.M. Brekelmans, F.P.T. Baaijens, Discrete ductile fracture modeling for the metal blanking process, Comput. Mech. 26 (2000) 104–114.
[24] A.M. Goijaerts, L.E. Govaert, F.P.T. Baaijens, Evaluation of ductile fracture models for different metals in blanking, J. Mater. Process. Technol. 110 (2001) 312–323.
[25] W. Klingenberg, U.P. Singh, FE simulation of the punching process using in-process characterization of mild steel, J. Mater. Process. Technol. 134 (2003) 296–302.
[26] V. Tvergaard, Material failure by void growth, Adv. Appl. Mech. 27 (1980) 83–147.
[27] N. Aravas, On the numerical integration of class of pressure-dependent plasticity models, Int. J. Num. Methods Eng. 24 (1987) 1395–1416.
[28] H.H. Wisselink, J. Huétink, Simulation of slitting process with FEM, Proceedings of the SheMet, 1999.
[29] M. Oyane, T. Sato, K. Okimoto, S. Shima, Criteria for ductile fracture and their applications, J. Mech. Work. Technol. 4 (1980) 65–81.
[30] M. Oyane, Criteria of ductile fracture strain, J. Soc. Mech. Eng. 15 (90) (1972) 1507–1513.
[31] W. Kubli, J. Reissner, Optimization of sheet-metal forming processes using the special-purpose program Auto Form. J. Mater. Process. Technol. 50 (1995) 292–305.
[32] ABAQUS Version 6.2, User's Manual, Hibbitt Karlsson and Sorensen Inc.
[33] S.E. Clift, P. Hartley, E.N. Sturgess, G.W. Rowe, Fracture prediction in plastic deformation processes, Int. J. Mech. Sci. 32 (1) (1990) 1–12.
[34] M. Li, S. Ghosh, O. Richmond, H. Weiland, T.N. Rouns, Three dimensional characterization and modeling of particle reinforced metal matrix composites. Part 1. Quantitative description of microstructural morphology, Mater. Sci. Eng. A 265 (1999) 153–173.
[35] E.R. Weibel, Stereological Methods: Theoretical Foundation, vol. 2, Academic Press, London, 1980.
[36] S. Roy, S. Ghosh, R. Shivpuri, A new approach to optimal design of multi-stage metal forming processes by micro genetic algorithms, Int. J. Machine Tools Manuf. 37 (1) (1997) 29–44.
[37] J.S. Chung, S.M. Hwang, Application of a genetic algorithm to process optimal design in non-isothermal metal forming, J. Mater. Process. Technol. 80/81 (1998) 136–143.